Letter Vol. 51, No. 20 / 15 October 2026 / Optics Letters 5673



Co-localized microwave-to-optical transduction via electrostatic actuation

Peiqin Chen,[1,2] Liping Zeng,[1,2] Yifei Zhang,[1,2] Hengrui Liang,[1,2] Chenglong You,[1,2] You Wang,[3] Haizhi Song,[3] Daquan Yang,[4] Guangcan Guo,[5] Jindao Tang,[1,2,6] and Guangwei Deng[1,2,*]

[1]Institute of Fundamental and Frontier Sciences, University of Electronic Science and Technology of China, 610054 Chengdu, China
[2]Key Laboratory of Quantum Physics and Photonic Quantum Information, (University of Electronic Science and Technology of China), Ministry of Education, Chengdu 611731, China
[3]Southwest Institute of Technical Physics, Chengdu 610054, China
[4]State Key Laboratory of Information Photonics and Optical Communications, School of Information and Communication Engineering, Beijing University of Posts and Telecommunications, Beijing 100876, China
[5]Key Laboratory of Quantum Information, University of Science and Technology of China, Hefei 230026, China
[6]jdtang@uestc.edu.cn
*gwdeng@uestc.edu.cn

Received 21 August 2026; revised 14 September 2026; accepted 14 September 2026; posted 16 September 2026; published 2 October 2026

Microwave-to-optical transduction bridges microwave photons used in superconducting quantum circuits and optical photons suitable for long-distance transmission, making it a key enabling technology for distributed quantum networks. Scalable implementation, however, requires device architectures that combine practical conversion performance with low fabrication complexity, whereas many existing approaches rely on heterogeneous material integration. Here, we demonstrate a co-localized microwave-to-optical transducer that integrates electrostatic excitation, mechanical mediation, and optical readout within a single optomechanical cavity. The electrostatic actuator is implemented using only a single metallization layer, reducing device complexity and avoiding the need for separate electromechanical and optomechanical resonators. This compact, fabrication-friendly architecture offers a practical route toward scalable integrated microwave photonics and future chip-scale microwave-to-optical interfaces for hybrid quantum systems. © 2026 Optica Publishing Group. All rights, including for text and data mining (TDM), Artificial Intelligence (AI) training, and similar technologies, are reserved.

https://doi.org/10.1364/OL.614943

Microwave-to-optical transduction provides an interface between microwave-frequency electronics and optical systems, enabling information processing in microwave photonics [1–3], quantum transduction [4–6], and hybrid quantum networks [7–9]. Compact and fabrication-friendly transducers are therefore desirable for both classical and quantum integrated systems.

Various approaches have been developed for microwave-to-optical transduction. Direct schemes rely on electro-optic nonlinearities [10], whereas phonon-mediated schemes use mechanical resonances with enhanced electromechanical and optomechanical interactions [4,11]. The latter often rely on piezoelectric actuation, but combining strong piezoelectric response with high optomechanical performance in a single material remains challenging. Heterogeneous integration can alleviate this trade-off, but adds fabrication steps and potentially lossy acoustic interfaces [12–16]. Recently, a piezoelectric-free silicon transducer connected a capacitive electromechanical resonator to a spatially separated optomechanical cavity through a phononic waveguide [17]. Although avoiding piezoelectric materials, this architecture requires complex narrow-gap electrode fabrication and inter-resonator frequency matching.

Here, we demonstrate electrostatically driven microwave-to-optical transduction using an integrated optomechanical cavity. Unlike previous architectures employing separated electromechanical and optomechanical components, our device uses a single localized mechanical mode for both electrostatic excitation and optical readout. This co-localized design eliminates the need for an intermediate phononic waveguide and enables a simplified planar electrostatic actuator defined by a single metallization layer. We systematically investigate the dependence of the transduction performance on optical detuning, optical power, microwave frequency, and DC bias voltage.

As shown in Fig. 1(a), the device consists of a suspended one-dimensional nanobeam optomechanical resonator positioned between a pair of electrodes. The operating principle is illustrated in Fig. 1(b). An RF signal and a DC bias are combined through a bias tee and applied across the electrodes to generate an oscillating electrostatic force:

$$F_{\Omega}(t) = \left.\frac{\partial C}{\partial x}\right|_{x_m} V_{\mathrm{DC}} V_{\mathrm{RF}} \cos(\Omega t), \tag{1}$$

where C is the displacement-dependent capacitance, x_m is the mechanical-displacement amplitude, and Ω is the microwave drive angular frequency. This force drives the localized mechanical mode resonantly when $\Omega \approx \Omega_m$. The mechanical displacement subsequently modulates the optical cavity resonance through optomechanical coupling, enabling microwave-

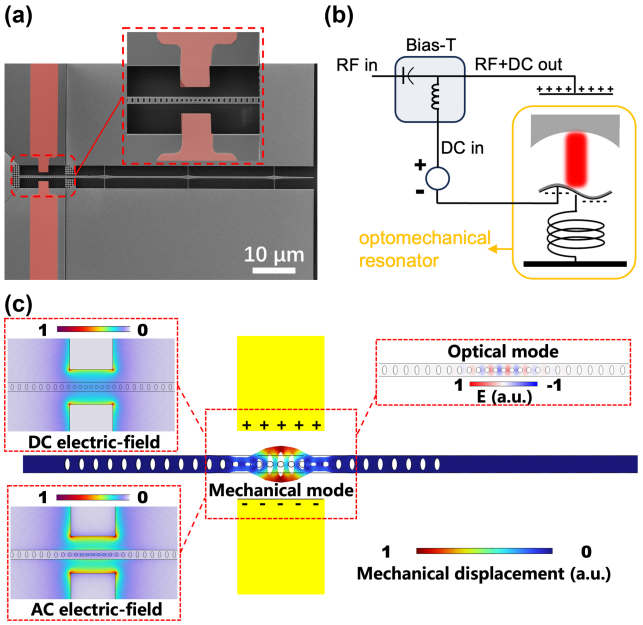


Fig. 1. Integrated optomechanical platform for co-localized microwave-to-optical transduction. (a) Scanning electron microscope (SEM) image of the fabricated device, showing the suspended mechanical resonator integrated with the optical cavity and electrostatic driving electrodes. (b) Schematic illustration of the transduction mechanism, where a microwave signal combined with a DC bias electrostatically drives the mechanical resonator. (c) Simulated optical mode, mechanical mode, and electric fields.

to-optical conversion when the probe laser is operated at an appropriate detuning.

Finite-element simulations confirm the spatial overlap between the localized mechanical mode, optical mode, and electric-field distribution, as shown in Fig. 1(c). Details of the device fabrication process are provided in Supplement 1.

Before measuring microwave-to-optical transduction, we first characterized the optical and mechanical responses of the fabricated optomechanical cavity. The optical response determines the probe condition and displacement-readout sensitivity, while the mechanical resonance sets the frequency and bandwidth of the electrically driven transduction. Figure 2(a) presents the optical transmission spectrum of the nanobeam optomechanical cavity. A Lorentzian fit to the resonance at 1564.825 nm yields an optical linewidth of 554.7 MHz and a loaded quality factor of 3.45×10^5. The measured high optical quality factor shows that good optical confinement is retained in the fabricated device with integrated electrodes. Because an otherwise identical cavity without electrodes was not measured, however, the present data do not independently quantify the perturbation introduced by the electrodes. The detailed experimental configuration used for optical and mechanical characterization is described in Supplement 1.

The mechanical characteristics of the device were subsequently investigated through optical detection. Figure 2(b) shows a pronounced resonance at 5.118 GHz, corresponding to the localized breathing mode of the optomechanical cavity. A Lorentzian fit yields a mechanical linewidth of 3.374 MHz and a quality factor of 1517. This resonance enhances the mechanically mediated transduction near its resonance frequency and provides a well-defined operating frequency. A higher

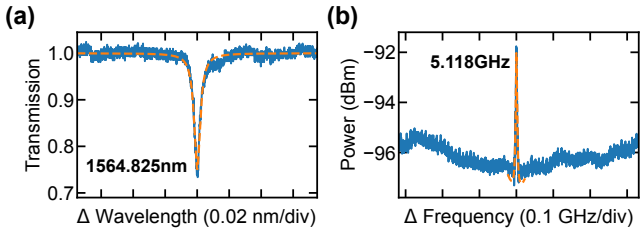


Fig. 2. Optical and mechanical characterization of the optomechanical cavity. (a) Optical transmission spectrum of the nanobeam cavity. (b) Measured mechanical spectrum of the localized breathing mode. In both panels, the blue traces represent the measurements, and the orange dashed curves represent the Lorentzian fits.

mechanical quality factor may be attainable under cryogenic operation.

Having established the optical and mechanical characteristics of the device, we next investigated how the optical readout conditions influence the microwave-to-optical transduction process. The probe-laser detuning and input optical power are varied separately while the electrical drive is held fixed.

The transduction process follows the standard dispersive optomechanical interaction [18], where mechanical displacement modifies the cavity resonance according to

$$\delta\omega_c = G_{\mathrm{om}} x_m, \tag{2}$$

where $G_{\mathrm{om}} = \partial\omega_c/\partial x$ is the optomechanical coupling coefficient. The resulting photocurrent modulation scales as

$$\delta I_{\mathrm{PD}} \propto P_{\mathrm{in}} \left(\frac{\partial T}{\partial \omega}\right) G_{\mathrm{om}} x_m, \tag{3}$$

where P_{in} is the input optical power, $T(\omega)$ is the cavity transmission, and δI_{PD} is the AC photocurrent generated by the mechanically induced optical modulation.

Figure 3(a) presents the measured microwave spectra obtained while tuning the laser wavelength across the optical cavity resonance. Here, the relative wavelength is defined as $\Delta\lambda = \lambda - 1564.8$ nm, so that $\Delta\lambda = 0$ corresponds to a probe wavelength of 1564.8 nm. This operating wavelength is 0.025 nm below the optical resonance wavelength of 1564.825 nm measured in Fig. 2(a). Throughout the wavelength scan, the mechanical resonance remains centered at approximately 5.118 GHz, whereas the detected signal power changes dramatically with laser wavelength. The absence of measurable changes in the mechanical resonance frequency and linewidth indicates that optomechanical dynamical backaction is below the measurement sensitivity within the investigated wavelength range. The observed power variation is therefore attributed primarily to the wavelength-dependent optical transduction slope $\partial T/\partial\omega$.

The extracted peak powers are summarized in Fig. 3(b). The transduction signal decreases by more than 36 dB as the laser wavelength moves away from the optimum detuning condition, consistent with the wavelength-dependent cavity transduction sensitivity.

The influence of the optical input power was further investigated at $\Delta\lambda = 0$. Representative RF spectra measured under different optical powers are shown in Fig. 3(c). Increasing the probe power directly increases the detected photocurrent modulation according to Eq. (3), without requiring a change in the underlying optomechanical response. The nearly unchanged

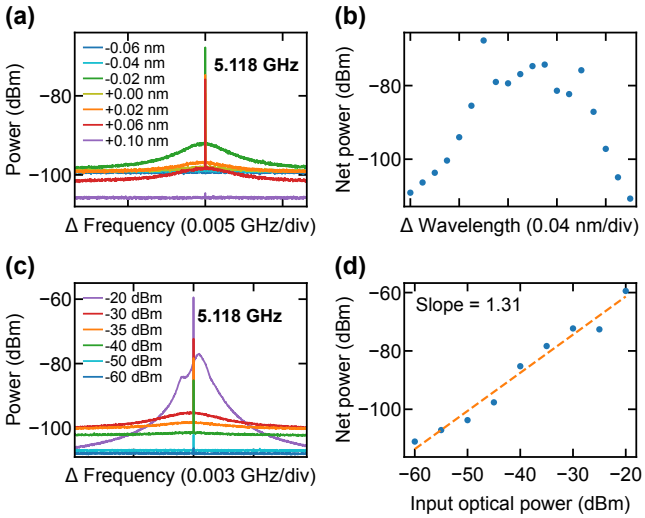


Fig. 3. Optical control of microwave-to-optical transduction. (a) Microwave spectra measured while tuning the laser wavelength across the optical cavity resonance, where $\Delta\lambda = \lambda - 1564.8$ nm. (b) Extracted peak RF transduction power as a function of relative wavelength. For (a) and (b), the input optical power is −30 dBm. (c) Microwave spectra measured under different input optical powers at a laser wavelength of 1564.8 nm ($\Delta\lambda = 0$). (d) Peak transduction power as a function of input optical power. For all panels, the microwave drive frequency and power are 5.118 GHz and 7 dBm, respectively, and the DC bias is 30 V. In (b) and (d), the blue circles represent the measurements; the orange dashed line in (d) represents the linear fit.

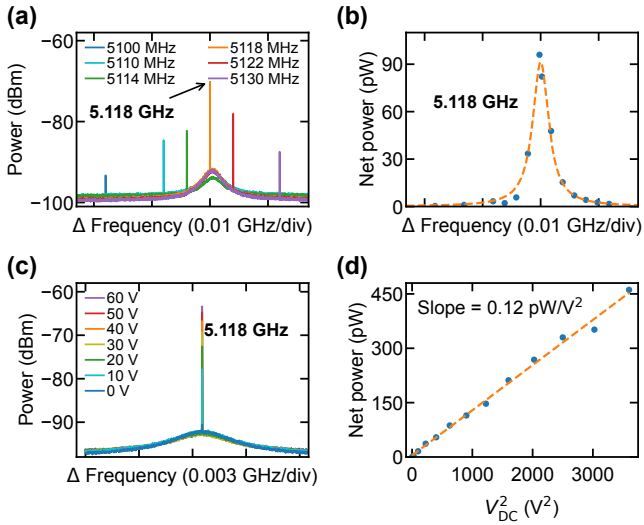


Fig. 4. Electrical control of the microwave-to-optical transduction. (a) Microwave spectra measured at different microwave driving frequencies. (b) Peak signal power extracted from the spectra in (a) as a function of microwave driving frequency. For (a) and (b), the microwave drive power is 7 dBm and the DC bias is 30 V. (c) Microwave spectra measured at different DC bias voltages with the microwave frequency fixed at 5.118 GHz. (d) Extracted net transduction signal power plotted as a function of V_{DC}^2. For (c) and (d), the microwave drive power is 7 dBm. For all panels, the laser wavelength and input optical power are 1564.8 nm and −30 dBm, respectively. In (b) and (d), the blue circles represent the measurements; the orange dashed curves represent the Lorentzian and linear fits, respectively.

resonance frequency and linewidth indicate that the mechanical response is not measurably modified over the investigated optical-power range.

The extracted background-subtracted peak powers are shown in Fig. 3(d). Increasing the optical power from −60 dBm to −20 dBm enhances the detected signal by approximately 47 dB, while the mechanical resonance remains unchanged. The fitted slope is 1.31, which is lower than the theoretical value of 2 expected for the detected RF power. This deviation may arise from the limited gain of the erbium-doped fiber amplifier (EDFA) over the investigated optical-power range. The signal increase therefore primarily reflects the direct scaling of the photocurrent modulation with probe power, rather than an intrinsic improvement in the optomechanical response or displacement-readout sensitivity.

These results demonstrate that optimizing the optical operating conditions maximizes the transduction signal without modifying the intrinsic mechanical response.

After optimizing the optical readout conditions, we investigated the influence of electrical driving parameters by tuning the microwave frequency and DC bias voltage.

Figure 4(a) presents the RF spectra of the photodetected optical signal recorded while sweeping the microwave driving frequency under the fixed operating conditions listed in the caption. A pronounced transduction signal is observed only when the driving frequency approaches the localized mechanical resonance, whereas the signal rapidly decreases away from resonance.

To quantitatively evaluate the frequency dependence, the peak powers extracted from the spectra are summarized in Fig. 4(b). The Lorentzian response is centered at approximately 5.118 GHz and has a linewidth of 3.33 MHz, in close agreement with the independently measured mechanical linewidth of 3.374 MHz in Fig. 2(b). This quantitative agreement shows that the frequency-dependent transduction is governed by the same localized nanobeam mechanical mode rather than by electrical feedthrough.

To further investigate the electrostatic actuation mechanism, the DC bias voltage was varied while maintaining the microwave frequency at 5.118 GHz. As shown in Fig. 4(c), the transduction signal increases continuously with increasing DC bias, while the resonance frequency remains essentially unchanged. This behavior indicates that the applied DC bias primarily strengthens the electromechanical driving force without measurably modifying the intrinsic mechanical resonance.

For electrostatic actuation, the driving force is given by

$$F_\Omega = \left(\frac{\partial C}{\partial x}\right) V_{DC} V_{RF}. \tag{4}$$

Under a fixed microwave excitation, the mechanical displacement is proportional to the driving force, i.e., $x_m \propto V_{DC}$. Since the optical modulation amplitude is proportional to the mechanical displacement and the detected RF power scales with the square of the modulation amplitude, the measured transduction signal satisfies

$$P_{det} \propto V_{DC}^2. \tag{5}$$

Figure 4(d) shows a linear dependence between the background-subtracted transduction signal and V_{DC}^2, confirming the electrostatic driving model. The detailed theoretical derivation of

the electrostatic driving and microwave-to-optical conversion process is provided in Supplement 1.

Finally, we evaluate the system-level microwave-to-optical conversion capability of the device. A representative photodetector RF spectrum was measured under a DC bias of 60 V and a microwave input power of 7 dBm (5.01×10^{-3} W). After subtracting the background in the linear-power domain, the detected RF signal power at the photodetector output is determined to be 4.61×10^{-10} W. We define the measured end-to-end power ratio as $P_{\mathrm{det,out}}/P_{\mathrm{RF,in}}$, where $P_{\mathrm{det,out}}$ is the background-subtracted RF power measured at the photodetector output and $P_{\mathrm{RF,in}}$ is the applied microwave source power. The resulting end-to-end power ratio is 9.2×10^{-8}. This system-level value includes the effects of optical amplification, optical-path losses, photodetector responsivity, and other uncalibrated losses in the measurement chain.

In summary, we have demonstrated microwave-to-optical transduction driven by electrostatic actuation within a single optomechanical cavity. The localized mechanical mode simultaneously mediates electrostatic excitation and optical readout, thereby co-localizing the electromechanical and optomechanical interactions within the same suspended cavity. This architecture eliminates the need for a separate electromechanical resonator and an intermediate phononic waveguide, while the planar electrostatic actuator requires only a single metallization layer. Systematic measurements reveal that the transduction is governed jointly by the optical readout conditions and the electrical driving parameters. Under the optimized operating conditions, a measured end-to-end power ratio of 9.2×10^{-8} is achieved. These results provide a compact and fabrication-friendly approach for integrated microwave photonics and chip-scale microwave-to-optical interfacing. Further improvements may be achieved through both optomechanical and electrical optimization. First, increasing the optical and mechanical quality factors would enhance the intracavity optical response and reduce mechanical dissipation, respectively. The mechanical quality factor could be improved by incorporating phononic shielding into the electrode and support structures to suppress acoustic leakage [17], while optimizing the optical coupling condition and improving the fiber-to-waveguide coupling efficiency would reduce optical insertion loss and increase the measured end-to-end conversion efficiency. Second, optimizing the electrode geometry could strengthen the electrostatic interaction, and integration with a microwave resonator, particularly a superconducting resonator under cryogenic operation [16], could improve impedance matching and resonantly enhance the local microwave voltage applied to the mechanical mode. Together, these improvements are expected to enhance both the intrinsic transduction performance and the system-level conversion efficiency.

Funding. Ministry of Science and Technology of the People's Republic of China (2022YFA1405900); Innovation Program for Quantum Science and Technology (2021ZD0302300); National Natural Science Foundation of China (92565107, U2441217, 92365112, 12574399, 12104236); Science and Technology Department of Sichuan Province (2024YFHZ0372); China Postdoctoral Science Foundation (2025M783362).

Disclosures. The authors declare no conflicts of interest.

Data availability. Data underlying the results presented in this paper are not publicly available at this time but may be obtained from the authors upon reasonable request.

Supplemental document. See Supplement 1 for supporting content.

REFERENCES

1. J. Capmany and D. Novak, Nat. Photonics **1**, 319 (2007).
2. J. Yao, J. Lightwave Technol. **27**, 314 (2009).
3. D. Marpaung, J. Yao, and J. Capmany, Nat. Photonics **13**, 80 (2019).
4. M. Mirhosseini, A. Sipahigil, M. Kalaee, *et al.*, Nature **588**, 599 (2020).
5. L. Fan, C.-L. Zou, R. Cheng, *et al.*, Sci. Adv. **4**, eaar4994 (2018).
6. X. Xu, Y. Zhang, J. Tang, *et al.*, Micromachines **15**, 485 (2024).
7. P. Kurpiers, P. Magnard, T. Walter, *et al.*, Nature **558**, 264 (2018).
8. S. Wehner, D. Elkouss, and R. Hanson, Science **362**, eaam9288 (2018).
9. X. Han, W. Fu, C.-L. Zou, *et al.*, Optica **8**, 1050 (2021).
10. M. Shen, J. Xie, Y. Xu, *et al.*, Nat. Photonics **18**, 371 (2024).
11. A. H. Safavi-Naeini, D. Van Thourhout, R. Baets, *et al.*, Optica **6**, 213 (2019).
12. X. Han, W. Fu, C. Zhong, *et al.*, Nat. Commun. **11**, 3237 (2020).
13. W. Jiang, C. J. Sarabalis, Y. D. Dahmani, *et al.*, Nat. Commun. **11**, 1166 (2020).
14. S. Hönl, Y. Popoff, D. Caimi, *et al.*, Nat. Commun. **13**, 2065 (2022).
15. S. Meesala, D. Lake, S. Wood, *et al.*, Phys. Rev. X **14**, 031055 (2024).
16. T. C. van Thiel, M. J. Weaver, F. Berto, *et al.*, Nat. Phys. **21**, 401 (2025).
17. H. Zhao, A. Bozkurt, and M. Mirhosseini, Optica **10**, 790 (2023).
18. M. Aspelmeyer, T. J. Kippenberg, and F. Marquardt, Rev. Mod. Phys. **86**, 1391 (2014).